Earth and Planetary Science Letters 432 (2015) 232–242

Contents lists available at ScienceDirect

Earth and Planetary Science Letters

www.elsevier.com/locate/epsl

Low steady-state stresses in the cold lithospheric mantle inferred from dislocation dynamics models of dislocation creep in olivine

Francesca Boioli [a], Andrea Tommasi [b], Patrick Cordier [a,*], Sylvie Demouchy [b], Alexandre Mussi [a]

[a] Unité Matériaux et Transformations, UMR 8207 CNRS - Université Lille 1, F-59655 Villeneuve d'Ascq, France
[b] Géosciences Montpellier - Université de Montpellier & CNRS, F-34095 Montpellier, France

ARTICLE INFO

Article history:
Received 4 July 2015
Received in revised form 28 September 2015
Accepted 6 October 2015
Available online 3 November 2015
Editor: J. Brodholt

Keywords:
olivine rheology
creep
deformation
lithospheric mantle
numerical modelling

ABSTRACT

Transmission electron microscopy observations on olivine crystals deformed at moderate (≤1273 K) temperature evidenced dislocations interactions explaining the hardening observed in the experiments, but also recovery mechanisms by the absorption or emission of point defects. Thus we investigate the possibility that, at geological strain-rates, these recovery processes allow steady-state deformation by dislocation creep at low to moderate temperatures in the lithospheric mantle. We test this hypothesis using a 2.5-D dislocation dynamics (DD) model, which combines dislocation glide and recovery by climb. This model shows that diffusion-controlled recovery processes allow for steady-state deformation by dislocation creep in the lithospheric mantle at stresses <500 MPa. For stresses of 50–200 MPa, steady-state strain-rates of 10^{-15} s^{-1} may be attained at temperatures as low as 900 K. Fitting of the DD model produces a flow law, which represents a lower bound for the lithospheric mantle strength, since the models describe the deformation of an olivine single crystal in an easy slip orientation. Comparison of strain-rates and Moho temperatures inferred for different geodynamic environments and the predictions of this model-based flow law implies, nevertheless, that, except in incipient rifts, most of the observed deformation may be produced by stress levels ≤200 MPa, consistent with those inferred to be produced by convection. This convergence suggests that the present models, which explicitly calculate the time-dependent dislocation dynamics, may provide a correct first order estimate of the mechanical behaviour of the lithospheric mantle, which cannot be derived directly from any existing data.

1. Introduction

The strength and the active deformation mechanisms in the lithospheric mantle are one of the major open questions in plate tectonics. Extrapolation of empirical flow laws derived from high-temperature (>1473 K) deformation experiments on olivine single-crystals and polycrystals to geological strain-rates (10^{-12} to 10^{-15} s^{-1}) predicts stresses largely exceeding 1 GPa in the cold uppermost levels of the lithospheric mantle. Indeed, for deforming the lithospheric mantle at temperatures of 873 K and strain-rates of 10^{-14} s^{-1}, anhydrous flow laws for olivine polycrystals predict stresses ranging from 1.6 GPa to 5.07 GPa (Fig. 1). Lower stresses (375–800 MPa) are predicted by extrapolation of hydrous high-temperature flow laws (Fig. 1), but these values probably overestimate both the water contents in olivine in the lithospheric mantle (Bell and Rossman, 1992; Ingrin and Skogby, 2000; Demouchy et al., 2006; Peslier, 2010) and the effect of water on the olivine rheology, which is probably limited to a reduction in strength by a factor 2–3 (Demouchy et al., 2012; Fei et al., 2014).

The predicted strength of a 100 km thick plate is therefore significantly higher than the stresses which may be produced in a viscoelastic lithosphere by mantle convection or those inferred by modelling the deformation in response to crustal loads, such as volcanic chains (100–200 MPa; *e.g.*, Beuchert and Podladchikov, 2010; Zhong and Watts, 2013). Yet, continental plates deform. This paradox may be partially solved by proposing that the cold uppermost lithospheric mantle deforms by brittle failure or low temperature plasticity (Fig. 1). When implemented in numerical models, flow laws simulating these processes and the associated thermal dissipation allow indeed successful simulation of many geodynamic processes, in particular continental breakup (*e.g.*, Brune, 2014). However, the rarity of mantle earthquakes in

* Corresponding author at: Université Lille 1, Unité Matériaux et Transformations, UMR CNRS 8207 - Bat C6, 59655 Villeneuve d'Ascq Cedex, France. Tel.: +33 320 434341.
E-mail address: Patrick.Cordier@univ-lille1.fr (P. Cordier).

http://dx.doi.org/10.1016/j.epsl.2015.10.012

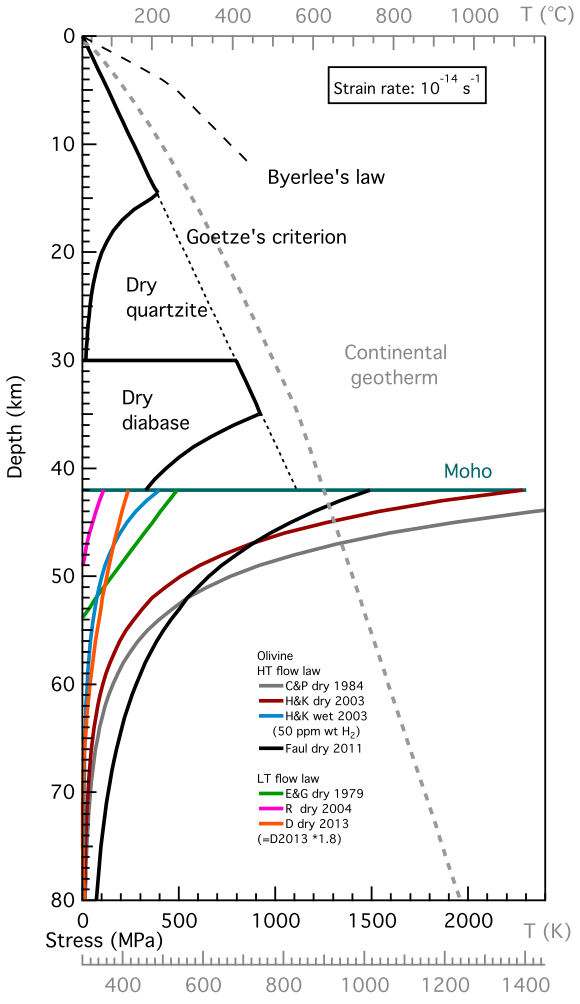

Fig. 1. Strength envelope model for a 100 km-thick continental lithosphere deforming at a vertically uniform strain-rate of 10^{-14} s^{-1}. The geotherm is plotted in grey. Yield stresses in the crust were calculated using: the frictional sliding law from Byerlee (1977) and Goetze's criterion with a density of 2700 $kg\,m^{-3}$; the flow law for anhydrous quartzite from Gleason and Tullis (1993); and the flow law for anhydrous diabase from Mackwell et al. (1998). In the mantle (below the Moho), are displayed: the low temperature flow laws from Demouchy et al. (2013), Raterron et al. (2004), and Evans and Goezte (1979), as well as the anhydrous and hydrous high temperature flow laws from Hirth and Kohlstedt (2003), the anhydrous high temperature flow law from Faul et al. (2011), and the anhydrous high temperature flow law from Chopra and Paterson (1984).

continental domains (Maggi et al., 2000; Jackson, 2002) tends to falsify the assumption of a cold mantle rheology controlled by frictional processes. Indeed, the rare earthquakes nucleating at sub-Moho depths beneath the Himalayas (Monsalve et al., 2006) or active rift zones (Lindenfeld and Rumpker, 2011) were ascribed to the underplating of the cold Indian lithosphere or to magma migration rather than tectonic processes.

On the other hand, the change from a power law to an exponential dependence of strain-rate on stress (*i.e.*, power law breakdown) is consistent with the few data on deformation of olivine single and polycrystals at temperatures <1300 K (Raleigh, 1968; Phakey et al., 1972; Durham and Goetze, 1977; Evans and Goetze, 1979; Raterron et al., 2004; Demouchy et al., 2009, 2013, 2014). These data also indicate that the shallow cold lithospheric mantle may deform at geological strain-rates under significantly lower stresses than predicted from the extrapolation of high-temperature data (Fig. 1). Indeed, at a temperature of 873 K and a strain-rate of 10^{-14} s^{-1}, the flow law from Demouchy et al. (2013) predicts stresses of ~270 MPa.

However, conducting deformation experiments on olivine at $T < 0.5T_m$ (T_m is the melting temperature, *i.e.* for olivine $Fo_{90} \approx$ 1973 K) suffers from major shortcomings. As temperature decreases, higher pressures are needed to avoid brittle deformation. Gas-medium apparatus, where confining pressures are limited to <500 MPa, provide accurate mechanical data, but do not allow to deform plastically olivine below 1100 K (Demouchy et al., 2013). Steady-state is rarely achieved in low temperature experiments; most stress strain-rate curves are characterised by marked strain hardening. Flow laws have been therefore established by fitting the data at a given strain, which is in all cases lower than the strain values expected in the mantle. Demouchy et al. (2013), for instance, used the maximum stress attained in each experiment, which corresponds to total shortenings ranging from 4.7 to 23.5%.

Below 1100 K, ductile deformation can only be achieved by applying high confining pressures, for instance using the D-DIA apparatus, which has high uncertainty in the stress data (Raterron et al., 2004; Long et al., 2011), or by using indentation measurements (Evans and Goetze, 1979), which give only indirect rheological information. In spite of these limitations, exponential flow laws, in particular the one from Evans and Goetze (1979), have been widely used to model the mechanical behaviour of the upper mantle. Yet, there are many reasons to question whether this strain-dependent data may be used to predict the mechanical behaviour of the uppermost lithospheric mantle in situations in which large deformations are expected, such as convergent plate boundaries, lithospheric scale shear zones and transform faults, or continental rifts.

In this article, we propose a new strategy to infer the rheology of olivine at low temperature and natural strain-rates by combining experimental data and numerical modelling of intracrystalline plasticity. First, we rely on a detailed analysis by Transmission Electron Microscopy (TEM) of the most recent low-temperature deformation experiments of olivine by Demouchy et al. (2013, 2014), which allow unravelling the elementary deformation mechanisms at work. These observations permit to identify the mechanisms, which lead to hardening and brittleness, but also to highlight the recovery processes, which are hindered at high strain-rates. These recovery processes are diffusion-driven and, thus, both time and temperature-dependent. At geological strain-rates, recovery should be much more effective than in the experiments, possibly allowing steady-state to be achieved. To test for this hypothesis, dislocation dynamics models are used to analyse the interplay between dislocation glide and diffusion-driven recovery processes, such as climb, in olivine. Within this model we can predict the steady-state strain-rates, which might be achieved at the stress-temperature conditions expected to prevail in the lithospheric mantle. These predictions, which represent a lower bound since we model the deformation of a well-oriented single crystal, not a polycrystal, are validated by comparison to strain-rates and Moho temperatures observed in a variety of geodynamic environments.

2. Experimental constraints

2.1. Deformation experiments

The rheology of mantle rocks at lithospheric temperatures has been essentially constrained by deformation experiments on olivine crystals and aggregates under variable confining pressures, from atmospheric (indentation experiments) to up to 3–8 GPa (D-DIA experiments), and temperatures (300–1623 K). Since the slow strain-rates relevant for geodynamics (10^{-12} s^{-1} to 10^{-18} s^{-1}) cannot be achieved in the laboratory, in mechanical testing of geomaterials time is often traded for temperature. However, the validity of this assumption is still to be tested.

Recently, tri-axial compression experiments on oriented single crystals of San Carlos olivine were performed at tempera-

tures relevant of the uppermost mantle (1073 to 1363 K; Demouchy et al., 2009, 2013). These experiments were carried out at a confining pressure of 300 MPa in a high-resolution gas-medium mechanical testing apparatus under constant strain-rates from 7×10^{-6} s^{-1} to 1×10^{-4} s^{-1}. Olivine cylinders with different crystallographic orientations (close to $[101]_c$, $[110]_c$ and $[011]_c$ orientations) were compressed in order to activate one or two of the dominant slip systems in olivine in each experiment, namely [100](001), [001](100) and [001](010), or [100](010). Final finite strains ranged from 4 to 23%. The experiments yielded differential stress often higher than the confining pressure: from 88 to 1076 MPa. Although high, these stresses are significantly lower than those predicted by the extrapolation of the flow laws derived from higher temperature experiments (1473–1573 K) to the present temperatures (Fig. 1). This result implies that time cannot be simply traded for temperature in study of the mechanical behaviour of the lithospheric mantle.

However, these fast strain-rate experiments at low temperature ($1073\ K = 0.47T_m$) under low confining pressure faced several limitations: stress hardening was observed in most experiments, the samples often broke before achieving a steady-state regime or even before 5% of strain, and stick-and-slip-like behaviour was occasionally observed (Demouchy et al., 2013). *Post mortem* study of the samples by EBSD revealed micro-fracturing superimposed to plastic deformation (Demouchy et al., 2013, 2014). These observations indicate transitional brittle–ductile deformation mechanisms at 1073 K and laboratory strain-rates. Older studies (Raleigh, 1968; Phakey et al., 1972; Evans and Goetze, 1979) despite using different approaches must have been confronted to the same limitations. In summary, below 1073 K, the current experimental methods for characterising the rheology of olivine reach their limits. New approaches are needed to properly determine the rheology of cold uppermost lithospheric mantle.

2.2. Transmission electron microscopy (TEM) analysis of the deformation mechanisms

The deformed crystals described above have been characterised by TEM. Doubly polished thin sections (30–25 μm thick) were glued on a Mo grid and ion milled at 5 kV under a low beam angle of 15° until electron transparency is reached. TEM observations were carried out using a Philips CM30 microscope operating at 300 kV and a FEI Tecnai G20 microscope operating at 200 kV. Dislocations microstructures have been analysed using weak-beam dark-field (WBDF) and electron tomography methods (Mussi et al., 2014, 2015a).

Here we summarise the observations made on all samples. Rather than emphasising the differences between samples deformed along different directions, we highlight the general trend and the deformation mechanisms which have been found to operate in every case. As expected, at *ca.* $0.5T_m$, evidence for glide of [001] dislocations on {110} and (100) planes predominates. If the crystals are not favourably oriented for activation of these slip systems, [001] dislocations glide in other {*hk*0} planes, but evidence for cross slip events in the easiest planes is common. In {110} and (100), non-screw segments slip much faster. Their curved shapes indicate that they bear little lattice friction (Fig. 2a). They leave behind long straight screw segments; their slower motion controls the glide strain-rates. Elastic interactions between non-screw segments result in dislocation dipoles, which are extremely common in the deformed samples (Fig. 2a and b). These dipoles are stable and form obstacles for other gliding dislocations, resulting in progressive building of entanglements (Fig. 2b and c). We interpret this mechanism as the primary source of hardening in olivine deformed at low temperature.

Despite the low temperature, we also observe pervasive evidence for onset of recovery mechanisms involving ionic diffusion. Every sample displays evidence for breakdown of dislocation dipoles into strings of prismatic loops (Fig. 2c). This well-known recovery mechanism, which has been described in ceramics deformed at high temperature (Junqua and Grilhé, 1984; Lagerlöf et al., 1989), works as follows. Under the influence of pipe diffusion, line instabilities develop along the dipole by self-climb. Eventually, these instabilities result in pinching of the dipole (Fig. 2d) and in formation of aligned prismatic loops. These loops progressively shrink and ultimately disappear by absorbing point defects that diffuse toward them. In fact, Goetze and Kohlstedt (1973) had already noticed the collapse of dislocation loops during high-temperature annealing experiments in olivine.

In samples deformed at laboratory strain-rates, that is, at 10^{-4} to 10^{-6} s^{-1}, these recovery mechanisms are not fast enough. The density of loops increases. The interactions of the loops with gliding dislocations create numerous non-glissile dislocation segments and contribute very efficiently to hardening as described in Mussi et al. (2015b). As a result, carrying deformation experiments at laboratory strain-rates becomes difficult at temperatures below 1273 K. Steady-state is not reached, instabilities develop, and the samples become brittle. An obvious hypothesis is that at geological strain-rates, that is, at 10^{-12} to 10^{-16} s^{-1}, recovery mechanisms may have enough time to operate and allow steady-state creep, but until which temperature and with which efficiency? In the following, we take advantage of recent developments in dislocations dynamics modelling to investigate this possibility.

3. Dislocation dynamics modelling

3.1. Description of the model

We use 2.5-Dimensional Dislocation Dynamics (2.5-D DD) simulations to model dislocation creep in olivine in temperature and stress ranges relevant for the lithospheric mantle. The present work follows the methodology recently established to study the high temperature ($T > 1400$ K) creep properties of olivine (Boioli et al., 2015). This previous study showed that the interplay between glide and climb dislocation motion leads to steady-state creep behaviour, following a power law that is in good agreement with high-temperature experimental data. The aim of the present models is to understand to which extent the interaction between glide and climb may allow steady-state creep at the low temperatures ($800\ K < T < 1400\ K$) which prevail in lithospheric mantle.

Discrete DD is a well-established simulation technique to describe the collective behaviour of dislocations and to model plastic flow in crystalline solids. In this method, the forces acting on dislocations are calculated using the linear elasticity theory. This provides a description of the long-range elastic strain field induced by dislocations, their reciprocal interaction, and the interaction of these line defects with an external stress field (Hirth and Lothe, 1992). These long- and short-range interactions are key ingredients to describe the collective behaviour of dislocations. Dislocations are then moved in the direction of the forces according to mobility laws, which take into account the relevant atomistic processes controlling dislocation motion (Devincre et al., 2011). In the 2.5-D dislocation dynamics model (Gomez-Garcia et al., 2006), dislocations are materialised by parallel straight segments perpendicular to a reference plane and their dynamics is followed only in the reference plane. Additional rules are included to reproduce important 3-D dislocation mechanisms, as dislocation multiplication, dipole annihilation or junction formation. First, a multiplication rule is used to reproduce the general observation that dislocation loops expand under an external loading and that,

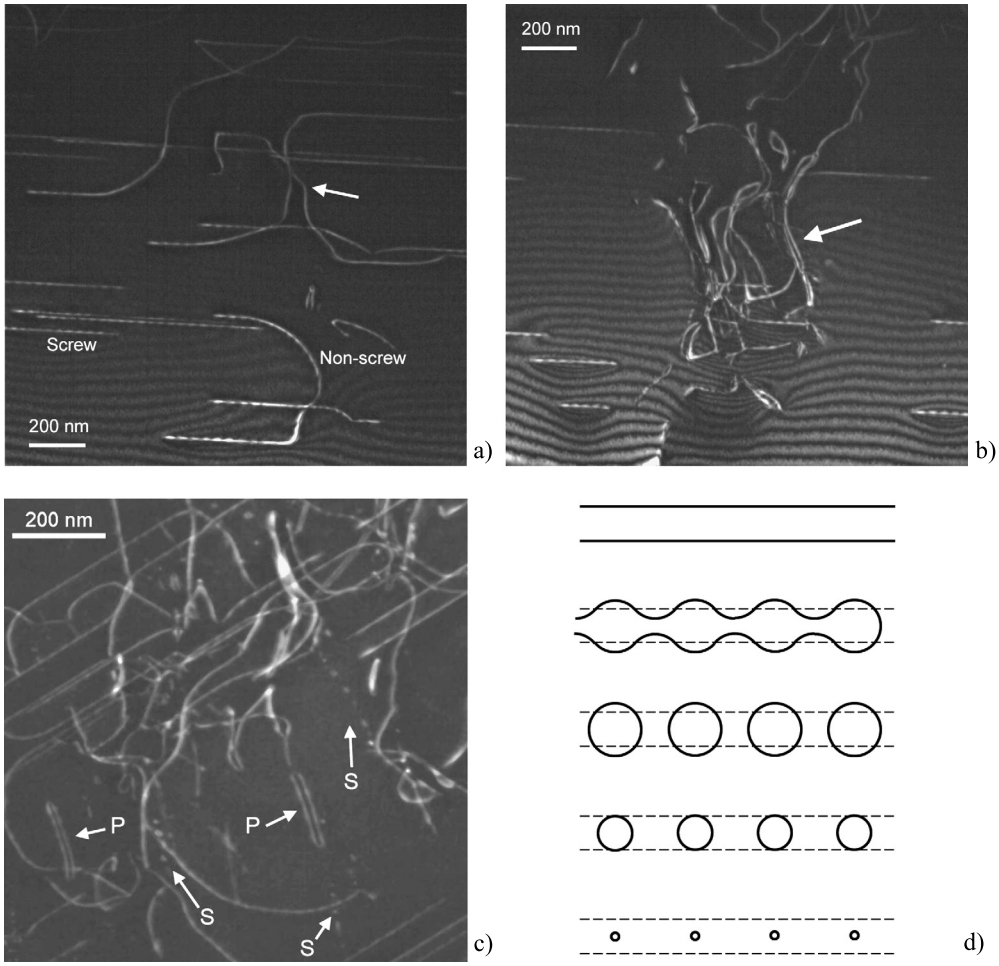

Fig. 2. TEM images of: (a) Olivine crystal POEM 19 deformed at 900 °C, $\dot{\varepsilon} = 1.01 \times 10^{-5}$ s^{-1} displaying straight [001] screw segments (horizontal) and curved non-screw segments that interact elastically (arrow). (b) POEM 19–900 °C, $\dot{\varepsilon} = 1.01 \times 10^{-5}$ s^{-1}. These interactions lead to the formation of stable dipoles (arrow), which eventually lead to the formation of entanglements. (c) POEM 11–850 °C, $\dot{\varepsilon} = 7.06 \times 10^{-6}$ s^{-1}. Within those entanglements, one can find evidence of recovery. Following the mechanism depicted in (d), dipoles pinch (P) and breakdown in strings (S) of sessile loops which shrink and disappear by diffusion. (d) Under the action of pipe diffusion, instabilities develop on the dislocation lines, which pinch and break up into sessile loops. The loops are sinks for point defects and progressively shrink and disappear as a result of bulk diffusion (after Junqua and Grilhé, 1984 and Lagerlöf et al., 1989).

as a consequence, the dislocation density ρ increases linearly with the plastic strain ε produced. Dislocation dipoles are inserted at random positions in the simulation box, provided that the local effective stress has the same sign of the external stress, according to the multiplication rate: $\mathrm{d}\rho/\mathrm{d}\varepsilon = m$, where m is a constant (Gomez-Garcia et al., 2006). This reflects the observation that most of the dislocations emerging in a reference plane, or slice, of a 3-D volume originate from sources in the surrounding volume. Here, the value $m = 2 \times 10^{15}$ m^{-2} has been taken to reproduce the evolution of the dislocation density modelled by 3-D-DD simulations (Durinck et al., 2007). Second we allow dislocations involved in a dipole to mutually annihilate when the distance between them is smaller than a critical distance $r_a = 10b$ (b is the Burgers vector modulus). These annihilation events result in a reduction of the dislocation density during the simulations. More details on the 2.5-D DD approach and the simulation settings for modelling olivine dislocation creep are presented in Boioli et al. (2015). In the following, we describe the glide and climb mobility laws used in the present model.

A key point to model dislocation creep is the description of the interplay between the glide velocity of dislocations in the most favourable crystallographic planes and the displacement rate of dislocations outside the glide planes by climb, *i.e.* the motion of dislocation induced by the absorption/emission of point defects, which controls recovery. In high lattice resistance materials, such as olivine, it is commonly assumed that plastic strain is controlled by the motion of slow screw segments left by the rapid propagation of non-screw segments with produce little strain. Screw dislocations move according to a thermally-activated kink-pairs mechanism and the overall dislocation glide velocity, which is limited by the motion of the screw segments, can be expressed by an Arrhenius rate equation (Kocks et al., 1975):

$$v_g = b\frac{L}{l_c}\nu_D\frac{b}{l_c}\exp\left(-\frac{\Delta H(\tau^*)}{k_B T}\right) \tag{1}$$

where L is the length of the dislocation, b is the modulus of the Burgers vector, l_c is the critical length for kink nucleation, ν_D is the Debye frequency, k_B is the Boltzmann constant, and T is the temperature (in K). $\Delta H(\tau^*) = \Delta H_0(1 - (\tau^*/\tau_P)^p)^q$ is the activation enthalpy of kink formation, which depends on the effective resolved shear stress τ^* (at each dislocation position $\tau^* = \tau_{app} + \tau_{int}$ is calculated as the sum of the applied stress and the elastic interaction stress induced by all the other dislocations, both projected along the slip direction). In the expression of $\Delta H(\tau^*)$, τ_P is the Peierls stress, *i.e.* the stress required to move dislocations at 0 K, ΔH_0 is the activation enthalpy at 0 stress, and p and q are empirical parameters. The glide mobility for [001] dislocations in the present simulations is defined using the parameters obtained by Durinck et al. (2007), which are reported in Table 1.

Table 1
Parameters used to define the glide mobility law for [001] dislocations as defined by Durinck et al. (2007).

τ_P (MPa)	p	q	ν_0 (m/s)	l_c (nm)	ΔH_0 (eV - kJ/mole V)
1730 ± 41	0.5988	1.1506	2.75×10^3	1.95	5.4 - 521

The second important mobility law is the one describing the climb velocity, which controls the elimination of the prismatic loops. Climb occurs through the absorption/emission of point defects (dominantly vacancies) by the dislocations. Here, we assume that the dislocation lines are saturated with jogs, *i.e.* steps along the dislocation lines in the climb direction, where vacancies can be absorbed or emitted instantaneously (with no activation barrier). Within this assumption the climb process is limited by diffusion of vacancies from the bulk to the dislocation (or vice-versa). Assuming steady-state conditions, the net flux of vacancies from and to the dislocation core is calculated by solving the diffusion equation; this allows an analytical expression of the climb velocity v_c to be derived (Hirth and Lothe, 1992; Martin and Caillard, 2003):

$$v_c = \eta \frac{D^{sd}}{b}\left[\exp\left(\frac{\tau_c^* \Omega}{k_B T}\right) - \frac{c_\infty}{c_0}\right] \quad (2)$$

where D^{sd} is the vacancy self-diffusion coefficient, Ω is the vacancy formation volume, η is a geometrical factor that depends on the geometry of the flux field, and c_∞ and c_0 are the vacancy concentration far from the dislocation and the equilibrium vacancy concentration in the bulk volume, respectively. Following Boioli et al. (2015), we assume that far away from the dislocations the vacancy concentration is constant and equal to the equilibrium concentration in the bulk volume ($c_\infty = c_0$). The climb process in olivine, which is an ionic crystal composed by four different elements, clearly involves the diffusion of several vacancy species. Here, since silicon is the slowest diffusing species, we consider that the diffusion rate is limited by the silicon self-diffusivity. Hence, in Eq. (2), $\Omega = 72.4$ Å^3, that is, the vacancy formation volume for a Schottky defect estimated from the unit cell volume of olivine, and $D^{sd} = D^{sd}_{Si} = D_0 \exp(\frac{\Delta H^{sd}_{Si}}{k_B T})$ is the self-diffusion coefficient of silicon taken from diffusion experiments at high pressure and high temperature. We have considered different sets of diffusion equations for Si self-diffusivity, obtained under both anhydrous and hydrous conditions, to span the maximum range of Si diffusion coefficient and environmental conditions to properly assess its influence on the calculated stresses. First, in analogy with the simulations reported in Boioli et al. (2015), we used the recent Si diffusivities for anhydrous, iron-free, forsterite from Fei et al. (2012), which yields for anhydrous conditions 3.74×10^{-24} m^2/s at 1273 K ($D_0 = 2.51 \times 10^{-7}$ m^2/s; $\Delta H^{sd}_{Si} = 4.25$ eV (410 kJ/mol), $\Delta V = 1.7$ cm^3/mol, ambient pressure). Second, we used the Si diffusivity for hydrous iron-bearing olivine from Costa and Chakraborty (2008), which yields for hydrous conditions 3.44×10^{-22} m^2/s at 1273 K ($D_0 = 1.68 \times 10^{-7}$ m^2/s; $\Delta H^{sd}_{Si} = 3.71$ eV (358 kJ/mol) $f_{water} = 0.98$ GPa), and for anhydrous olivine ($\sim$Fo$_{93}$) from Dohmen et al. (2002), which yields 1.78×10^{-26} m^2/s at 1273 K ($D_0 = 6.31 \times 10^{-5}$ m^2/s; $\Delta H^{sd}_{Si} = 5.48$ eV (529 kJ/mol)). The value for the Si diffusion activation enthalpy in anhydrous forsterite reported in Fei et al. (2012) is comparable with the one measured in iron-bearing olivine, $\Delta H^{sd}_{Si} = 4.03 \pm 0.31$ eV (389 kJ/mol) (Karato and Ogawa, 1982), but smaller than the value reported by Dohmen et al. (2002), $\Delta H^{sd}_{Si} = 5.48 \pm 0.42$ eV (529 kJ/mol). A reduced efficiency of the recovery processes is expected if the latter diffusivity data are considered. An upper and a lower bound estimate of strain-rates was obtained by using Si diffusivity data measured for hydrous and anhydrous olivine, respectively.

3.2. Creep simulations

In order to address the plastic behaviour at lower strain-rates, we performed creep simulations by coupling glide and climb dislocation motion. In all simulations, we imposed single slip and uniaxial loading conditions on a single crystal. The geometry of the simulation box is sketched in Fig. 3a. The loading axis is parallel to the y direction and it forms an angle of 45° with the glide direction and with the normal to the glide plane. The climb displacement direction is perpendicular to the glide one. Different box dimensions: $L = L_x = L_y$, between 2 and 8 μm, and different initial dislocation density values ρ_0, between 10^{12} and 2×10^{13} m^{-2}, have been considered. In particular, ρ_0 has been set to be, approximately, from 3 to 10 times smaller than the equilibrium dislocation density predicted for a given creep stress in the considered temperature regime as in Boioli et al. (2015).

In Fig. 3, we compare the dislocation microstructure and the stress field induced by both the dislocation microstructure and the external loading predicted by DD models in which only glide was activated or where glide was coupled to recovery by climb. Both models were run for a temperature of 1100 K and an applied stress of 50 MPa. In the initial configuration (Fig. 3b), dislocations are randomly distributed. An initial dislocation density $\rho_0 = 2.5 \times 10^{12}$ m^{-2} is assumed in both runs. The final dislocation density is $\rho = 6 \times 10^{12}$ m^{-2} in the glide only models (Fig. 3c). It is lower, $\rho = 5.5 \times 10^{12}$ m^{-2}, when climb is activated (Fig. 3d). During the deformation process, dislocations with similar sign tend to align perpendicularly to the glide direction creating sub-grain boundaries, which can be seen in the final configuration of both models (arrows in Fig. 3c and d). However, the most common features in the microstructure are pairs of dislocations with opposite signs, forming dipoles. In Fig. 3c and d, we highlight a few dipoles with circles, but most dislocations are involved in dipole interactions.

The analysis of the strain *vs.* time curves (Fig. 4) shows that when dislocations are restricted to move by glide only, after a short transient, they become trapped in dipoles, blocking any further plastic strain production if stress is not increased. The effect of climb is to eliminate these "jammed" configurations, allowing for steady-state deformation. Indeed, glide produces dislocation multiplication, whereas climb promotes dipole annihilation. At the steady-state, the dislocation density fluctuates around an equilibrium value, denoting balance between these competing mechanisms. This is in agreement with the creep behaviour of olivine predicted in the high temperature regime (Boioli et al., 2015) and demonstrates the importance of the climb mechanism even at moderate temperature.

First, we performed a few simulations in the conditions where experiments were done to check for the validity of the model before addressing the deformation behaviour at geological strain-rates (10^{-12}–10^{-15} s^{-1}), relevant for the lithospheric mantle. The first tests were carried out at a constant strain-rate of 10^{-5} s^{-1} and for 800 K $\leq T \leq$ 1400 K. The predicted flow stresses are consistent with the experimental mechanical data, as we can see in Fig. 5a where the calculated stresses corresponding to a shortening $\varepsilon = 2\%$ (empty boxes) are compared with the experimental values (circles). Under those conditions, diffusion processes are too slow to sustain such high strain-rates and glide is the dominant deformation mechanism. At larger deformations ($\varepsilon > 2\%$), strain hardening due to the interaction of dislocation in different glide planes occurs. Here we do not focus on the plastic behaviour in this advanced deformation stage because the 2.5-DD simulations are not well adapted to describe the hardening observed in most

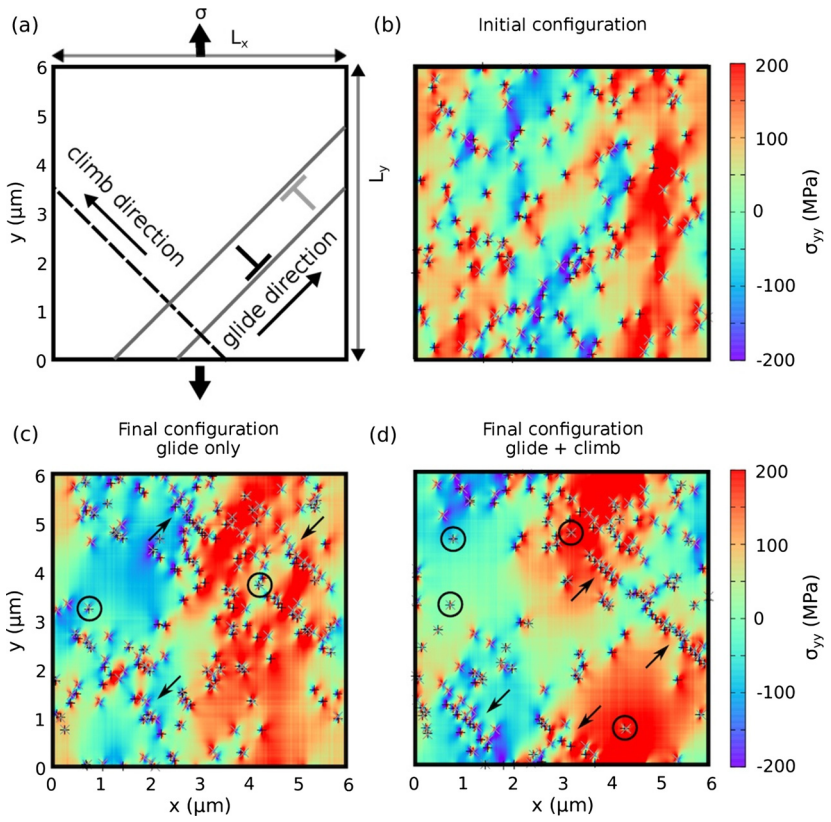

Fig. 3. (a) Sketch of the 2D simulation box. Single slip conditions and uniaxial loading along the y direction (loading direction) are applied. The angle between the loading axis and glide direction is 45°. Dislocations (plus or multiplication symbols) are superimposed on a colour background, which represents the component σ_{yy} of the stress field induced by the dislocation microstructure and the imposed external forces. (b) Initial configuration. (c, d) Final dislocation microstructure in a model with glide only (c) and in which glide is coupled with climb (d). Arrows indicate sub-grain boundaries formed by arrays of dislocations. The dislocation density ρ is equal to 2.5×10^{12} m^{-2} in (b; initial dislocation density) and to 6×10^{12} m^{-2} and 5.5×10^{12} m^{-2} in panels (c) and (d), respectively (end of simulation dislocation densities, which are quasi stationary in (d), but still evolving in (c)).

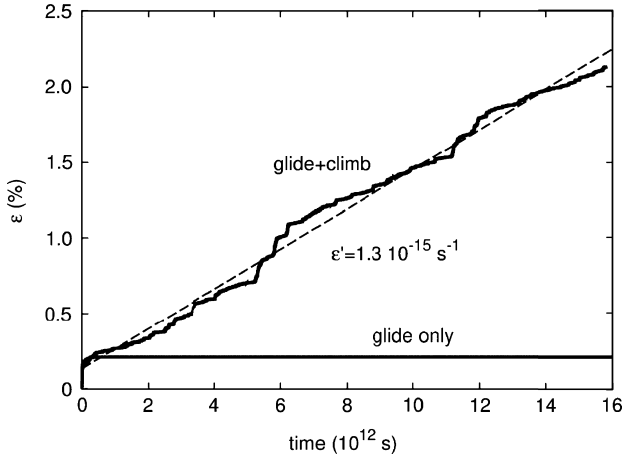

Fig. 4. Plastic deformation ε *vs.* time, obtained in creep conditions ($\sigma = 50$ MPa, $T = 1100$ K), assuming glide only (solid grey line) and glide coupled with climb (solid black line) dislocation motion. The average slope of the black line represents the steady-state strain-rate (dashed line).

low-temperature experiments. The complexity of dislocation interactions under these high-stress conditions are not fully captured in the present model. 2.5-DD simulations produce, however, precise estimates of the critical stresses implied in dislocation glide. The agreement between the simulated and experimentally measured mechanical behaviour at low finite strains in the high strain-rate regime substantiates the predictive power of the 2.5-D DD model and justifies the use of this method to predict the flow stresses in the low strain-rate regime.

A larger set of simulations has then been performed under constant load in order to calculate the creep strain-rate in olivine in the temperature range between 800 and 1400 K. For each temperature, we performed several simulations by increasing the applied stress from 43 to 500 MPa. Each simulation was run up to steady-state conditions. Creep rates were determined by a linear least-square fit of plastic strain *vs.* time curves, as the one shown in Fig. 4. The results are plotted in Fig. 5 (flow stresses calculated at 10^{-14} s^{-1} as a function of temperature), Fig. 6 (strain-rate as a function of temperature), and Fig. 7 (strain-rate as a function of stress).

4. Discussion of DD simulation results

The main question addressed in the present study is whether steady-state dislocation creep may be attained at low to moderate temperatures in the upper mantle. At high temperature, diffusion processes are fast and climb is expected to occur. In olivine, DD simulations performed between 1400 K and 1700 K confirmed that climb is a key mechanism to reach steady-state conditions (Boioli et al., 2015). Climb governs the rate at which dislocations bypass obstacles or at which dislocation dipoles annihilate, controlling the steady-state. However, recovery mechanisms promoted by diffusion may operate even at intermediate/low temperature and fast strain-rates, as indicated by the TEM data in Fig. 2, which displays evidence for breakdown of dislocation dipoles into strings of prismatic loops induced by the absorption/emission of point defects. Here, we show that steady-state creep is observed down to 800 K even under low stresses (50 MPa). In this extreme case, steady-state strain-rates are extremely low ($\sim 10^{-18}$ s^{-1}) and do

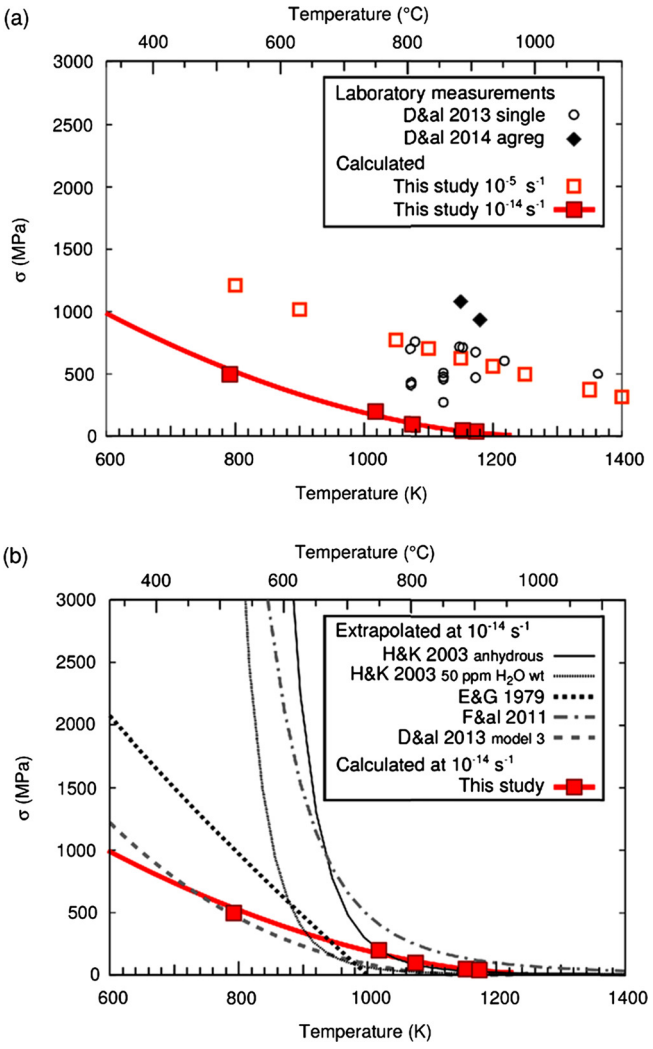

Fig. 5. Critical flow stress σ as a function of the temperature T. (a) Flow stresses obtained by 2.5-D DD simulations for strain-rates of 10^{-5} (empty boxes) and of 10^{-14} s^{-1} (full boxes) compared with mechanical data for olivine single crystals from Demouchy et al. (2013) (circles, D&al2013 single crystals) and olivine aggregate from Demouchy et al. (2014) (diamonds, D&al2014 agreg). The flow law derived from the 2.5-D DD results at 10^{-14} s^{-1} is shown as solid line. (b) Flow stress calculated by 2.5-D DD model and the resulting flow law compared with models obtained by extrapolating the experimental results from laboratory strain-rates to 10^{-14} s^{-1} strain-rate from H&K: Hirth and Kohldstedt (2003) in anhydrous and hydrous conditions, E&G1979: Evans and Goetze (1979), F&al2011: Faul et al. (2011), D&al2013: model 3 from Demouchy et al., 2013.

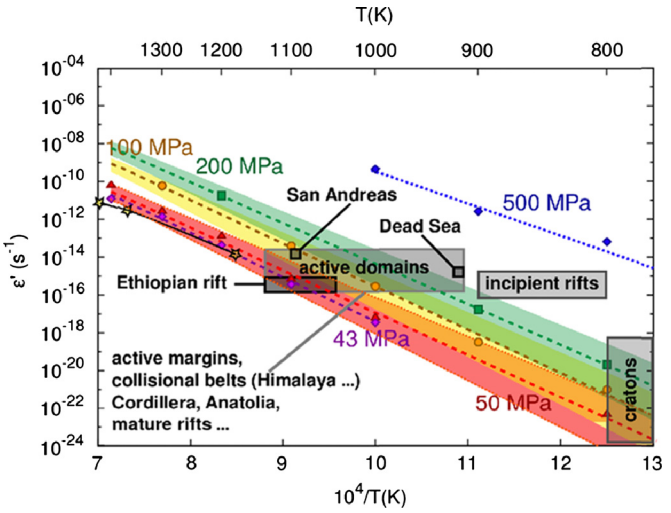

Fig. 6. Calculated 2.5-D DD strain-rate values $\dot{\varepsilon}$ as a function of the reciprocal temperature T. Colours indicate calculations for different stresses. The creep strain-rates obtained by using the Si self-diffusion coefficient measured in anhydrous forsterite (Fei et al., 2012) are shown by full symbols and dashed lines ($D_0 = 2.51 \times 10^{-7}$ m^2/s and $\Delta H_{Si}^{sd} = 4.25$ eV (410 kJ/mol)). The upper and the lower limits of the coloured bands represent the 2.5-D DD results obtained by considering the Si self-diffusion coefficient values of: $D_0 = 1.68 \times 10^{-7}$ m^2/s and $\Delta H_{Si}^{sd} = 3.71$ eV (358 kJ/mol) (Costa and Chakraborty, 2008) and $D_0 = 6.31 \times 10^{-5}$ m^2/s; $\Delta H_{Si}^{sd} = 5.48$ eV (529 kJ/mol) (Dohmen et al., 2002), for anhydrous and hydrous olivine, respectively. Squares delimitate strain-rate – temperature conditions inferred for lithospheric plates in different geodynamic situations (see text for details).

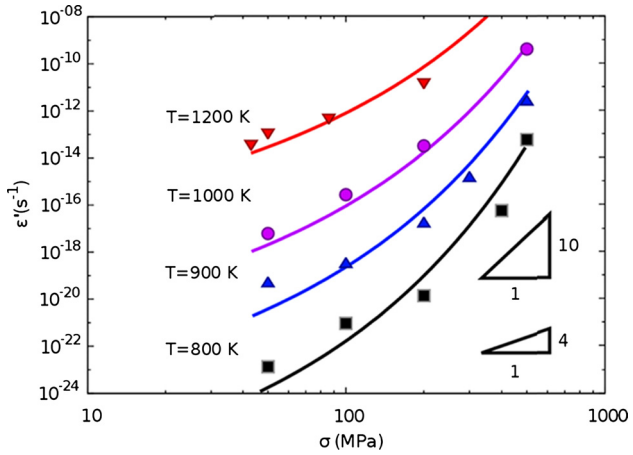

Fig. 7. Calculated 2.5-D DD strain-rate values $\dot{\varepsilon}$ as a function of the applied creep stress σ. Full lines show the fit obtained using Eq. (5), with $A' = 0.002$ and the glide parameters as defined in Table 1.

not produce deformations measurable by geodetic tools. This result demonstrates, however, that, when time is available, interplay between glide and climb may result in steady-state deformation even under very low temperatures (800 K $= 0.35 T_m$).

Analysis of the full dataset allows further examining the interplay between climb and glide and their respective influence on the creep strain-rates. In the temperature range considered in our simulations (800–1400 K), climb controls the steady-state strain-rate up to stresses of 200 MPa. The dislocation creep behaviour in this 'climb-controlled' regime is illustrated in Fig. 3 and 4. A fraction of mobile dislocations moves by glide until they reach a quasi-equilibrium configuration. Thanks to climb events, some dislocations escape from such 'jammed' configurations, become mobile, and produce further plastic strain. This succession of events is periodically repeated in time leading to steady-state conditions, *i.e.* a linear increase of the plastic deformation with time (constant strain-rate). In this regime the dislocation density fluctuates around an equilibrium value, which depends only on the applied creep stress. The influence of climb becomes less important with increasing applied stresses. In the simulations where a stress of 500 MPa is imposed, we observe that climb events are rare. However, while the climb velocity depends linearly on stress, the glide velocity increases exponentially with it (see Eqs. (1) and (2)), eventually allowing to reach large deformations before dislocation–dislocation interactions become important and 'jam' the microstructure. Thus, although climb events are rare in the simulations where a stress of 500 MPa is imposed, steady-state strain-rates are achieved, because the stress level is high enough to allow dislocations to bypass local attractive or repulsive configurations without the absorption or emission of point defects. These high-stress simulations were carried out up to strains of 10% without development of a 'quasi-equilibrium' dislocation configuration that would require climb to overcome obstacles and sustain the plastic flow.

At high temperatures, creep strain-rates are commonly analysed by using a power law equation:

$$\dot{\varepsilon} = A\sigma^n \exp\left(-\frac{Q}{k_B T}\right) \quad (3)$$

where Q is the creep activation enthalpy, σ the applied stress and T the temperature (in K). Q, n and A are assumed to be constant and depend on the physical mechanism controlling the macroscopic creep for a given material. To characterise the creep activation enthalpy, we plot the creep strain-rates obtained from the DD simulations as a function of the reciprocal temperature (Fig. 6). The curves of the logarithm of the strain-rate as a function of the reciprocal temperature present the same negative slope, indicating a constant activation enthalpy Q for creep in the examined stress range. By averaging the values for different stresses, we obtain $Q = 5.2 \pm 0.3$ eV (502 ± 29 kJ/mol), which is in agreement with the activation energy determined in high temperature creep ($Q \sim 5.4$ eV $= 520$ kJ/mol, Kohlstedt and Goetze, 1974; $Q \sim 4.7$ eV $=$ 453 kJ/mol, Gueguen and Darot, 1982; $Q \sim 4.9$ eV $= 470$ kJ/mol, Mei and Kohlstedt, 2000) and in numerical simulations ($Q =$ 5.07 eV $= 489$ kJ/mol, Boioli et al., 2015). The Q value extracted from the simulations lies between the activation barriers for climb, here equivalent to the Si self-diffusion enthalpy (410 kJ/mol) and for glide motion of [001] dislocations (521 kJ/mol).

In order to illustrate the influence of the diffusion coefficient on our results, we compare the creep strain-rates obtained by using the Si self-diffusion coefficient measured in anhydrous forsterite (Fei et al., 2012), dashed lines in Fig. 6, and the one measured in olivine for hydrous (Costa and Chakraborty, 2008) and anhydrous (Dohmen et al., 2002) conditions. We observe an increase of the strain-rates and a decrease of the activation enthalpy Q when Si diffusivity data for hydrous conditions are considered. The opposite behaviour (decrease of the strain-rates and an increase of the activation enthalpy Q) is predicted when Si diffusivity data for olivine in anhydrous condition are used. This shift is shown in Fig. 6 by using colour bands. The lower and the upper limit of the bands represent the strain-rate values for olivine under anhydrous and hydrous conditions, respectively. We notice that, even if the diffusion coefficient measured by Costa and Chakraborty, 2008 (Dohmen et al., 2002) is ~2 orders of magnitude larger (lower) than the one measured by Fei et al. (2012) at $T = 1273$ K, we observe an increase (decrease) of the strain-rates values by a factor of 2–4 at 50 MPa and by less than 1 order of magnitude at 800 K and 50 MPa, conditions at which we observe the maximum shift in the strain-rate values. This highlights that, to evaluate the effect of the diffusion coefficient on the strain-rates, the interplay between glide and climb must be considered and that estimating creep strain rates by simply assuming a linear relationship between strain-rates values and diffusion coefficient is not possible. At low stress ($\leq$200 MPa), when climb plays a key role in the plastic deformation process, the faster Si diffusion coefficient reported for hydrous conditions enhances the recovery processes and produces larger strain-rates. On the contrary, at high stress (500 MPa), we observe no influence of the Si diffusion coefficient on the strain-rates. This confirms that, at these high stresses, climb is not effective and dislocation motion by glide controls the creep properties of olivine.

In Fig. 7, the evolution of the strain-rate as a function of stress is plotted for different temperatures. A power law behaviour would result in straight lines. As expected, the predicted dependence of the strain-rate on stress in the temperature range of 800–1200 K deviates from the power law behaviour observed at higher temperature. Above 1400 K a constant stress exponent $n \sim 3$–3.5 is obtained for experiments in a wide range of stress conditions (Jin et al., 1994; Bai et al., 1991; Hirth and Kohlstedt, 2003) and it is assumed to characterise dislocation creep behaviour in olivine. A similar stress exponent, $n \sim 3 \pm 0.2$, is obtained by 2.5-D DD simulations of olivine creep behaviour at temperatures >1400 K and applied stress <100 MPa (Boioli et al., 2015). However, at low temperature, the creep behaviour of olivine cannot be modelled by a power law since the apparent stress exponent n would increase from 3.5 to 10 when the applied stress is increased from 50 to 500 MPa (Fig. 7) at 1000 K and to even larger values at 800 and 900 K.

Mechanical properties of olivine at low temperature are better described by introducing the dependence of strain-rates on stress within the exponential term:

$$\dot{\varepsilon} = A \exp\left(-\frac{Q}{k_B T}\left(1 - \left(\frac{\sigma}{\sigma_P}\right)^p\right)^q\right) \quad (4)$$

where k_B is the Boltzmann constant, σ_P is the Peierls stress and p and q are empirical parameters (*e.g.*, Evans and Goetze, 1979). This equation is assumed to be more adapted when plastic flow is controlled by glide involving lattice friction. By using Orowan's equation we can express the strain-rate as a function of the dislocation density ρ and the average dislocation velocity: $\dot{\varepsilon} = \rho b \bar{v}$. By further assuming that the average dislocation velocity is proportional to the glide velocity we can rewrite Eq. (4) as follows:

$$\begin{aligned}\dot{\varepsilon} &= \rho b \bar{v} = \rho b A' v_g \\ &= A' \rho b v_0 \exp\left(-\frac{Q}{k_B T}\left(1 - \left(\frac{0.5\sigma}{\sigma_P}\right)^p\right)^q\right)\end{aligned} \quad (5)$$

where p, q, σ_P, and Q are the parameters used to describe the glide velocity v_g (Eq. (1)) reported in Table 1, v_0 is the pre-exponential factor in the expression of v_g, b is the Burgers vector modulus, ρ is the dislocation density, and A' is a fitting parameter. In Eq. (5), we set the resolved shear stress $\tau = 0.5\sigma$, that is, the applied stress σ reduced by the Schmid factor. Following Boioli et al. (2015), we assume that the relationship between the equilibrium dislocation density ρ and the stress is given by $\rho = (\frac{0.5\sigma}{\mu})^s C'/b^2$, with the stress exponent $s = 1.31$ and $C' = 0.104$. Then, the remaining adjustable parameter A' is fitted to reproduce the modelled dependence of the strain-rates on stress, as illustrated in Fig. 7. By fitting these data (full symbols in Fig. 7) we find $A' = 0.002 \pm 0.0003$. The curves in Fig. 7 are obtained by plotting Eq. (5) for temperatures varying from 800 K to 1200 K using the values defined above. The correct fit of the results of the model for different stresses and temperatures with a single parameter set indicates that it is possible to describe the average dislocation velocity as the glide velocity reduced by a scaling factor (A'). This reflects the observation that dislocations can be trapped in dipole interactions and need to be released by climb in order to flow from one "jammed" configuration to another one. We notice that, in the examined (T, σ) range, the dependence of the strain-rate on the applied stress is mainly governed by the dependence of the glide velocity on the stress. In fact, by assuming a constant average dislocation density $\rho = 3 \times 10^{13}$ m^{-2}, we can still reproduce quite well the DD simulation results.

In order to propose a new flow law for the lithospheric mantle, we focus on the numerical results at strain-rates of 10^{-14}, which are relevant for the lithospheric mantle. The curve obtained by substituting $A' = 0.002$ in Eq. (5) (other parameters as in Table 1) and by assuming an average dislocation density $\rho = 3 \times 10^{13}$ m^{-2} is shown with a solid line in Fig. 5. This flow law obtained by fitting the results of the model represents a lower bound for the strength of an olivine rock at moderate to low temperature, since we model the deformation of a single crystal in an easy glide orientation, not of an olivine-rich rock, composed by crystals with a variety of orientations. Comparison between experimental data for olivine crystals and polycrystals at moderate temperature (circles

and diamonds in Fig. 5a, respectively) shows that the polycrystals are stronger by a factor two or less. A similar difference is obtained by analysing the high-temperature data (*e.g.*, Mackwell et al., 1985). Thus the model-based flow law probably underestimates the strength of a mantle rock, but by a factor two or less. It probably captures the correct order of magnitudes of stresses and strain-rates in the lithospheric mantle. We emphasize that the novelty of our model is to take into account diffusion-driven recovery processes, which, based on our simulation results, are expected to be important for stresses $\leq$200 MPa even at moderate temperature ($T \sim 0.35T_m$). Flow laws based on extrapolation of mechanical data from laboratory to geological strain-rates cannot capture the influence of such processes that are negligible at laboratory strain-rates. This explains the discrepancy between the 2.5-D DD model results and existing flow laws based on the extrapolation of experimental data from laboratory to geological strain-rates, shown in Fig. 5b.

5. Geodynamic implications

The 2.5 DD models substantiate the intuitive prediction that if recovery processes are already active during low temperature deformation experiments at strain-rates of 10^{-5} s^{-1}, at much slower geological strain-rates, diffusional processes are effective enough to allow for steady-state dislocation creep even in the shallow levels of the lithospheric mantle. At laboratory strain-rates, the strengths predicted by these models are lower by a factor 2 than those obtained using the exponential flow law of Demouchy et al. (2013), corroborating that this flow law represents an upper bound for the strength of the lithospheric mantle (Demouchy et al., 2014).

To evaluate if the predictions of these models are consistent with the strain-rates observed in nature, we plotted in Fig. 6 strain-rates calculated based on GPS data (Kreemer et al., 2014) and Moho temperatures for a variety of geodynamic environments. This simple approach, which implicitly assumes vertically homogeneous strain-rates within a plate, allows by comparison with the model predictions at the same conditions, to verify if the observed strain-rates may be produced by stress levels consistent with those estimated from plate boundary forces analyses or convection models ($\leq$200 MPa). In most cases, this condition is satisfied. Cratonic environments are characterised by extremely low temperatures at Moho depths (<800 K constrained by xenoliths thermobarometry, heat flow data, and Pn-velocities in a variety of cratons; *e.g.* Boyd, 1973; Brazier et al., 2000; Mareschal and Jaupart, 2004; McKenzie et al., 2005; Hyndman et al., 2009; Schutt et al., 2011; Baptiste et al., 2012). Consistently, they do not deform (non-measurable strain-rates, *i.e.* $<10^{-18}$ s^{-1}). High strain-rates ($>10^{-15}$ s^{-1}) are observed in active collisional boundaries, such as the Himalayas, the Andes, the Alps, the Cordillera, or Anatolia (Kreemer et al., 2014). All these domains are characterised by high Moho temperatures, ranging between 900 and 1100 K (Calvert et al., 2000; Al-Lazki et al., 2004; Liang and Song, 2006; Hyndman et al., 2009; Díaz et al., 2013). The present models indicate that at such temperatures, strain-rates of 10^{-14} s^{-1} to 10^{-15} s^{-1} may be attained for stresses in the range 50–200 MPa, that is, for stress levels consistent with those produced by mantle convection. Low Pn velocities indicating high Moho temperatures (>900 K; Buehler and Shearer, 2012) and high strain-rates ($>10^{-14}$ s^{-1}; Kreemer et al., 2014) also characterise the San Andreas fault and the mature domains of the East African rift system, such as the Afars (Mechie et al., 1994).

In contrast, incipient continental rifts, in which extension affects thick and hence cold plates, such as the southern part of the East African rift, where high P-wave velocities and xenolith data indicates Moho temperatures 800–900 K (Henjes-Kunst and Altherr, 1992; Mechie et al., 1994; Brazier et al., 2000; Baptiste et al., 2015), are characterised by strain-rates $>10^{-16}$ s^{-1}, which, accordingly to the present models cannot be produced by stresses $\leq$200 MPa. Thus, if the present models predict correctly the rheology of the shallow lithospheric mantle, additional softening processes, such as localised advective heating by magma percolation (Baptiste et al., 2015), or geometrical softening due to preferred orientation of olivine in the lithospheric mantle (Tommasi et al., 2009) are needed for allowing the initiation of continental rifting.

As an additional test of the models, we compare their predictions with temperature and paleopiezometric data derived from the analysis of peridotitic mylonites from the Beni Bousera massif in the Rif belt, Morocco (Frets et al., 2014). These mylonites constitute the upper part of a km-scale shear zone, which accommodated *ca.* 30 km of thinning of the lithospheric mantle in a transtensional setting. Paleothermometry data on these rocks indicate that they equilibrated at temperatures ranging between 1173 and 1473 K. Recrystallised grain sizes for the low-temperature mylonites are in the range 100–150 μm, which correspond, based on the paleopiezometer of Van der Wal et al. (1993), to stresses of 30–40 MPa. 2.5 DD models predict, for such temperatures and stresses, strain-rates of *ca.* 10^{-14} s^{-1} (Fig. 6). These values are lower by a factor 10 than those inferred for this shear zone based on thermal considerations (preservation of a temperature gradient of >200 K/km; Frets et al., 2014). Yet, much higher strain-rates, consistent with the preserved thermal gradient, are predicted for the coarse-grained peridotites, which accommodated the latter stages of the functioning of the shear zone (Frets et al., 2014). Similarly, if we use the present models to estimate the strain-rates in California based on paleothermometric and paleopiezometric data for mantle xenoliths in the Cima Volcanic field in California (1150–1220 K and stresses <20 MPa; Behr and Hirth, 2014), we obtain strain-rates of 10^{-14}–10^{-15} s^{-1}, which are consistent with those derived from GPS data for this region (Kremeer et al., 2014).

In summary, although the model-based flow law is a lower bound for the strength of the lithospheric mantle, the predicted behaviour of the shallow mantle is remarkably consistent with geological observations. It is also more coherent than the previous flow laws with the low strength of the shallow subcontinental lithosphere inferred from the analysis of post-seismic deformation (*e.g.*, Freed et al., 2012). Models of the flexure associated with Hawaii predict even lower strengths in the shallow and cold suboceanic mantle (Zhong and Watts, 2013). The very low strengths inferred from these data are nevertheless difficult to reconcile with our present knowledge of deformation mechanisms in olivine-rich rocks. Deformation of most of the subcontinental lithospheric mantle at stresses $\leq$200 MPa as predicted by the present models may have multiple implications for the thermo-mechanical evolution of the plates. Softening processes such as shear heating and grain size reduction would be less effective. Brittle processes should not be activated. On the other hand, extension of the dislocation creep field to lower temperatures would imply development of olivine crystal preferred orientations and, hence, anisotropy in the shallow subcontinental lithospheric mantle.

6. Conclusions

Recent deformation experiments on olivine single crystals and polycrystals showed that olivine-rich rocks have much lower strengths than those predicted from the extrapolation of high-temperature, low-stress experimental data (Demouchy et al., 2013, 2014). This observation falsifies the common assumption that a temperature enhancement may compensate for the high strain-rates in the experiments, calling for new data on the rheology of the lithospheric mantle. However, deformation experiments on olivine at temperatures <1273 K have many shortcomings. In particular, steady-state is almost never reached, most data showing

a continuous hardening up to activation of brittle deformation processes. Nevertheless, TEM analysis of deformed olivine single crystals deformed under low/intermediate temperature evidences dislocation interactions producing hardening, but also their partial recovery by the absorption or emission of point defects. As diffusion is a time-dependent process, we propose that at geological strain-rates these recovery processes allow steady-state deformation by dislocation creep at low to moderate temperatures in the lithospheric mantle.

We tested this hypothesis using a dislocation dynamics model, which associates dislocation glide and recovery by climb. This model shows that diffusion-controlled recovery processes allow for steady-state deformation by dislocation creep in the lithospheric mantle. If reasonable stress levels (50–200 MPa) are considered, steady-state strain-rates of 10^{-15} s^{-1} may be attained at temperatures as low as 900 K. Fitting of the DD model produces a flow law, which represents a lower bound for the lithospheric mantle strength, since the models simulate the deformation of an olivine crystal in an easy slip orientation. Experimental data at both moderate and high temperature indicate that an olivine polycrystal may be up to two times stronger than single crystals. Comparison of strain-rates and Moho temperatures inferred for different geodynamic environments and the predictions of this model-based flow law imply that, except in incipient rifts, most of the observed deformation may be produced by stress levels $\leq$200 MPa, consistent with those inferred to be produced by convection. Model predictions are also consistent with direct estimates of stresses and temperatures in naturally deformed mantle peridotites and the inferred strain-rates for each context. In summary, there is a clear need, if we want to correctly model the mechanical behaviour of the lithospheric mantle, to go beyond a simple extrapolation of laboratory data to geological strain-rates. The present study illustrates how modelling of the dislocation interactions may help constraining this scale transfer (10 orders variation in strain-rate).

Acknowledgements

A Marie Curie fellowship awarded to S.D. (PoEM: Plasticity of Earth Mantle, FP7-PEOPLE-20074-3-IRG, N°230748-PoEM) supported the experimental work used in this study. This work was supported by funding from the European Research Council under the Seventh Framework Program (FP7), ERC grant N°290424 – RheoMan to P.C. The TEM national facility in Lille is supported by the CNRS (INSU) and the Conseil Régional du Nord Pas de Calais, France. The manuscript benefited from careful reviews and useful comments from R. Dohmen and I. Jackson.

References

Al-Lazki, A.I., Sandvol, E., Seber, D., Barazangi, M., Turkelli, N., Mohamad, R., 2004. On tomographic imaging of mantle lid velocity and anisotropy at the junction of the Arabian, Eurasian and African plates. Geophys. J. Int. 158, 1024–1040.

Bai, Q., Mackwell, S.J., Kohlstedt, D.L., 1991. High-temperature creep of San Carlos olivine: 1. Steady-state flow laws. J. Geophys. Res. 96, 2441–2463.

Baptiste, V., Tommasi, A., Demouchy, S., 2012. Deformation and hydration of the lithospheric mantle beneath the Kaapvaal craton, South Africa. Lithos 149, 31–50.

Baptiste, V., Vauchez, A., Tommasi, A., Demouchy, S., Rudnick, R., 2015. Deformation, hydration, and anisotropy of the lithospheric mantle beneath an active rift: constraints from mantle xenoliths from the North Tanzanian Divergence. Tectonophysics 639, 34–55. http://dx.doi.org/10.1016/j.tecto.2014.1011.1011.

Behr, W.M., Hirth, G., 2014. Rheological properties of the mantle lid beneath the Mojave region in southern California. Earth Planet. Sci. Lett. 393, 60–72.

Bell, D.R., Rossman, G.R., 1992. Water in Earth's mantle: the role of nominally anhydrous minerals. Science 255, 1391–1397.

Beuchert, M.J., Podladchikov, Y.Y., 2010. Viscoelastic mantle convection and lithospheric stresses. Geophys. J. Int. 183, 35–63.

Boioli, F., Devincre, B., Marquille, M., Carrez, Ph., Cordier, P., 2015. Modelling the creep properties of olivine by 2.5-D dislocation dynamics simulations. Phys. Rev. B 92, 014115.

Boyd, F.R., 1973. A pyroxene geotherm. Geochim. Cosmochim. Acta 37, 2533–2538.

Brazier, R.A., Nyblade, A.A., Langston, C.A., 2000. On wave velocities beneath the Tanzania craton and adjacent mobile belts, East Africa. Geophys. Res. Lett. 27, 2365–2368.

Brune, S., 2014. Evolution of stress and fault patterns in oblique rift systems: 3-D numerical lithospheric-scale experiments from rift to breakup. Geochem. Geophys. Geosyst. 15, 3392–3415.

Buehler, J., Shearer, P., 2012. Localized imaging of the uppermost mantle with USArray Pn data. J. Geophys. Res. 117, B09305. http://dx.doi.org/10.1029/2012JB009433.

Byerlee, J.D., 1977. Friction of rocks. In: Proceedings of the Second Conference on Experimental Study of Rock Friction with Application to Earthquake Prediction. Menlo Park, California.

Calvert, A., Sandvol, E., Seber, D., Barazangi, M., Vidal, F., Alguacil, G., Jabour, N., 2000. Propagation of regional seismic phases (Lg and Sn) and Pn velocity structure along the Africa–Iberia plate boundary zone: tectonic implications. Geophys. J. Int. 142, 384–408.

Chopra, P.N., Paterson, M.S., 1984. The role of water in the deformation of dunite. J. Geophys. Res. 89, 7861–7876.

Costa, F., Chakraborty, S., 2008. The effect of water on Si and O diffusion rates in olivine and implications for transport properties and processes in the upper mantle. Phys. Earth Planet. Inter. 166, 11–29. http://dx.doi.org/10.1016/j.pepi.2007.10.006.

Demouchy, S., Jacobsen, S.D., Gaillard, F., Stern, C.R., 2006. Rapid magma ascent recorded by water diffusion profiles in mantle olivine. Geology 34, 429–432.

Demouchy, S., Mussi, A., Barou, F., Tommasi, A., Cordier, P., 2014. Viscoplasticity of polycrystalline olivine experimentally deformed at high pressure and 900 °C. Tectonophysics 623, 123–135.

Demouchy, S., Schneider, S.E., Mackwell, S.J., Zimmerman, M.E., Kohlstedt, D.L., 2009. Experimental deformation of olivine single crystal at lithospheric temperature. Geophys. Res. Lett. 36, L04304.

Demouchy, S., Tommasi, A., Barou, F., Mainprice, D., Cordier, P., 2012. Deformation of olivine in torsion under hydrous conditions. Phys. Earth Planet. Inter. 202–203, 56–70.

Demouchy, S., Tommasi, A., Boffa-Ballaran, T., Cordier, P., 2013. Low strength of Earth's uppermost mantle inferred from tri-axial deformation experiments on anhydrous olivine crystals. Phys. Earth Planet. Inter. 220, 37–49. http://dx.doi.org/10.1016/j.pepi.2013.04.008.

Devincre, B., Madec, R., Queyreau, S., Gatti, R., Kubin, L., 2011. In: Mechanics of Nano-Objects. Presse de l'Ecole des Mines de Paris, Paris, p. 85.

Díaz, J., Gil, A., Gallart, J., 2013. Uppermost mantle seismic velocity and anisotropy in the Euro-Mediterranean region from Pn and Sn tomography. Geophys. J. Int. 192, 310–325.

Dohmen, R., Chakraborty, S., Becker, H.W., 2002. Si and O diffusion in olivine and implications for characterizing plastic flow in the mantle. Geophys. Res. Lett. 29, 26, 4 pp.

Durham, W.B., Goetze, G., 1977. Plastic flow of oriented single crystals of olivine. 1. Mechanical data. J. Geophys. Res. 82, 5737–5753.

Durinck, J., Devincre, B., Kubin, L., Carrez, Ph., Cordier, P., 2007. Modeling the plastic deformation of olivine by dislocation dynamics simulations. Am. Mineral. 92, 1346–1357.

Evans, B., Goetze, C., 1979. The temperature variation of hardness of olivine and its implication for polycrystalline yield stress. J. Geophys. Res. 84, 5505–5524.

Faul, U.H., Fitz Gerald, J.D., Farla, R.J.M., Ahlefeldt, R., Jackson, I., 2011. Dislocation creep of fine-grained olivine. J. Geophys. Res. 116, B01203.

Fei, H., Hegoda, C., Yamazaki, D., Wiedenbeck, M., Yurimoto, H., Shcheka, S., Katsura, T., 2012. High silicon self-diffusion coefficient in anhydrous forsterite. Earth Planet. Sci. Lett. 345, 95–103.

Fei, H., Wiedenbeck, M., Yamazaki, D., Katsura, T., 2014. No effect of water on oxygen self-diffusion rate in forsterite. J. Geophys. Res. 119, 7598–7606.

Freed, A.M., Hirth, G., Behn, M.D., 2012. Using short-term postseismic displacements to infer the ambient deformation conditions of the upper mantle. J. Geophys. Res. 117, B01409.

Frets, E.C., Tommasi, A., Garrido, C.J., Vauchez, A., Mainprice, D., Targuisti, K., Amri, I., 2014. The Beni Bousera Peridotite (Rif Belt, Morocco): an oblique-slip low-angle shear zone thinning the subcontinental mantle lithosphere. J. Petrol. 55, 283–313.

Gleason, G.C., Tullis, J., 1993. Improving flow laws and piezometers for quartz and feldspar aggregates. Geophys. Res. Lett. 20, 2111–2114.

Goetze, C., Kohlstedt, D.L., 1973. Laboratory study of dislocation climb and diffusion in olivine. J. Geophys. Res. 78, 5961–5971.

Gomez-Garcia, D., Devincre, B., Kubin, L., 2006. Dislocation patterns and similitude principle: 2.5 D mesoscale simulations. Phys. Rev. Lett. 96, 125503.

Gueguen, Y., Darot, M., 1982. Upper mantle plasticity from laboratory experiments. Phys. Earth Planet. Inter. 29, 51–57.

Henjes-Kunst, F., Altherr, R., 1992. Metamorphic petrology of xenoliths from Kenya and northern Tanzania and implications for geotherms and lithospheric structures. J. Petrol. 33, 1125–1156.

Hirth, G., Kohlstedt, D.L., 2003. Rheology of the upper mantle and the mantle wedge: a view from the experimentalists. In: Inside the Subduction Factory. AGU Press, pp. 83–105.
Hirth, J.P., Lothe, J., 1992. Theory of Dislocations. Wiley.
Hyndman, R., Currie, C., Mazzotti, S., Frederiksen, A., 2009. Temperature control of continental lithosphere elastic thickness, Te versus Vs. Earth Planet. Sci. Lett. 277, 539–548.
Ingrin, J., Skogby, H., 2000. Hydrogen in nominally anhydrous upper-mantle minerals: concentration levels and implications. Eur. J. Mineral. 12, 543–570.
Jackson, J., 2002. Faulting, flow, and the strength of the continental lithosphere. Int. Geol. Rev. 44, 39–61.
Jin, Z.M., Bai, Q., Kohlstedt, D.L., 1994. High temperature creep of olivine crystals from four localities. Phys. Earth Planet. Inter. 82, 55–64.
Junqua, N., Grilhé, J., 1984. Apparitions d'instabilités sur des dipôles de dislocations coin. Acta Metall. 32, 2139–2147.
Karato, S., Ogawa, M., 1982. High-pressure recovery of olivine: implications for creep mechanisms and creep activation volume. Phys. Earth Planet. Inter. 28, 102–117.
Kocks, U.F., Argon, S., Ashby, F., 1975. In: Thermodynamics and Kinetics of Slip. Pergamon Press, Oxford.
Kohlstedt, D.L., Goetze, C., 1974. Low-stress high-temperature creep in olivine single crystals. J. Geophys. Res. 79, 2045–2051.
Kreemer, C., Blewitt, G., Klein, E.C., 2014. A geodetic plate motion and global strain-rate model. Geochem. Geophys. Geosyst. 15, 3849–3889.
Lagerlöf, K.P.D., Mitchell, T.E., Heuer, A.H., 1989. Energetics of the break-up of dislocation dipoles into prismatic loops. Acta Metall. 37, 3315–3325.
Liang, C., Song, X., 2006. A low velocity belt beneath northern and eastern Tibetan Plateau from Pn tomography. Geophys. Res. Lett. 33.
Lindenfeld, M., Rümpker, G., 2011. Detection of mantle earthquakes beneath the East African Rift. Geophys. J. Int. 186, 1–5.
Long, H., Weidner, D.J., Li, L., Chen, J., Wang, L., 2011. Deformation of olivine at subduction zone conditions determined from in situ measurements with synchrotron radiation. Phys. Earth Planet. Inter. 186, 23–35.
Mackwell, S.J., Kohlstedt, D.L., Paterson, M.S., 1985. The role of water in the deformation of olivine single crystals. J. Geophys. Res. 90, 11319–11333.
Mackwell, S.J., Zimmerman, M.E., Kohlstedt, D.L., 1998. High-temperature deformation of anhydrous diabase with application to tectonics on Venus. J. Geophys. Res. 103, 975–984.
Maggi, A., Jackson, J., McKenzie, D., Priestley, K., 2000. Earthquake focal depths, effective elastic thickness, and the strength of the continental lithosphere. Geology 28, 495–498.
Mareschal, J.C., Jaupart, C., 2004. Variations of surface heat flow and lithospheric thermal structure beneath the North American craton. Earth Planet. Sci. Lett. 223, 65–77.
Martin, J.L., Caillard, D., 2003. Thermally Activated Mechanisms in Crystal Plasticity. Pergamon.
McKenzie, D., Jackson, J., Priestley, K., 2005. Thermal structure of oceanic and continental lithosphere. Earth Planet. Sci. Lett. 233, 337–349.
Mechie, J., Fuchs, K., Altherr, R., 1994. The relationship between seismic velocity, mineral composition and temperature and pressure in the upper mantle with an application to the Kenya Rift and its eastern flank. Tectonophysics 236, 453–464.
Mei, S., Kohlstedt, D.L., 2000. Influence of water on the plastic deformation of olivine aggregates: 1. Diffusion creep regime. J. Geophys. Res. 105, 21457–21469.
Monsalve, G., Sheehan, A., Schulte-Pelkum, V., Rajaure, S., Pandey, M., Wu, F., 2006. Seismicity and one-dimensional velocity structure of the Himalayan collision zone: earthquakes in the crust and upper mantle. J. Geophys. Res. 111.
Mussi, A., Cordier, P., Demouchy, S., Vanmansart, C., 2014. Characterization of the glide planes of the [001] screw dislocations in olivine using electron tomography. Phys. Chem. Miner. 41, 537–545.
Mussi, A., Nafi, M., Demouchy, S., Cordier, P., 2015a. On the deformation mechanism of olivine single crystals at low temperatures: an electron tomography study. Eur. J. Mineral. http://dx.doi.org/10.1127/ejm/2015/0027-2481, in press.
Mussi, A., Cordier, P., Demouchy, S., 2015b. Characterization of dislocation interactions in olivine using electron tomography. Philos. Mag. 95, 335–345.
Peslier, A.H., 2010. A review of water contents of nominally anhydrous minerals in the mantles of Earth, Mars and the Moon. J. Volcanol. Geotherm. Res. 197, 239–258.
Phakey, P., Dollinger, G., Christie, J., 1972. Transmission electron microscopy of experimentally deformed olivine crystals. In: Heard, H.C., Borg, I.Y., Carter, N.L., Rayleigh, C.B. (Eds.), Flow and Fracture of Rocks. American Geophysical Union, Washington, DC, pp. 117–138.
Raleigh, C.B., 1968. Mechanisms of plastic deformation of olivine. J. Geophys. Res. 73, 5391–5407.
Raterron, P., Wu, Y., Weidner, D.J., Chen, J., 2004. Low-temperature olivine rheology at high pressure. Phys. Earth Planet. Inter. 145, 149–159.
Schutt, D., Buehler, C.J., Dueker, S.K., Lowry, A., 2011. Lithospheric Temperatures in the Western US. Institute on the Lithosphere Asthenosphere Boundary, Portland, OR. Sep. 19–21.
Tommasi, A., Knoll, M., Vauchez, A., Signorelli, J., Thoraval, C., Logé, R., 2009. Structural reactivation in plate tectonics controlled by olivine crystal anisotropy. Nat. Geosci. 2, 423–427. http://dx.doi.org/10.1038/ngeo528.
Van der Wal, D., Chopra, P., Drury, M.R., FistGerald, J., 1993. Relationships between dynamically recrystallized grain size and deformation conditions in experimentally deformed olivine rocks. Geophys. Res. Lett. 20, 1479–1482.
Zhong, S., Watts, A., 2013. Lithospheric deformation induced by loading of the Hawaiian Islands and its implications for mantle rheology. J. Geophys. Res., Solid Earth 118, 6025–6048.